

Graduate Texts in Physics

Ernst Meyer  
Roland Bennewitz  
Hans J. Hug

# Scanning Probe Microscopy

The Lab on a Tip

*Second Edition*

 Springer

Ernst Meyer  
Department of Physics  
University of Basel  
Basel, Switzerland

Roland Bennewitz  
Leibniz Institute for New Materials gGmbH  
INM  
Saarbrücken, Germany

Hans J. Hug  
Empa  
Dübendorf, Zürich, Switzerland

ISSN 1868-4513  
Graduate Texts in Physics

ISSN 1868-4521 (electronic)

ISBN 978-3-030-37088-6

ISBN 978-3-030-37089-3 (eBook)

<https://doi.org/10.1007/978-3-030-37089-3>

1<sup>st</sup> edition: © Springer-Verlag Berlin Heidelberg 2004

2<sup>nd</sup> edition: © Springer Nature Switzerland AG 2021

This work is subject to copyright. All rights are reserved by the Publisher, whether the whole or part of the material is concerned, specifically the rights of translation, reprinting, reuse of illustrations, recitation, broadcasting, reproduction on microfilms or in any other physical way, and transmission or information storage and retrieval, electronic adaptation, computer software, or by similar or dissimilar methodology now known or hereafter developed.

The use of general descriptive names, registered names, trademarks, service marks, etc. in this publication does not imply, even in the absence of a specific statement, that such names are exempt from the relevant protective laws and regulations and therefore free for general use.

The publisher, the authors and the editors are safe to assume that the advice and information in this book are believed to be true and accurate at the date of publication. Neither the publisher nor the authors or the editors give a warranty, expressed or implied, with respect to the material contained herein or for any errors or omissions that may have been made. The publisher remains neutral with regard to jurisdictional claims in published maps and institutional affiliations.

This Springer imprint is published by the registered company Springer Nature Switzerland AG  
The registered company address is: Gewerbestrasse 11, 6330 Cham, Switzerland

*This book is dedicated to Hans-Joachim  
Güntherodt who has been a great tutor and  
has supported many young scientists in this  
field.*

---

## Preface

Three decades after its invention, scanning probe microscopy has become a widely used method in laboratories as diverse as industrial magnetic storage development or structural biology. Consequently, the community of users ranges from biologists and medical researchers to physicists and engineers, all of them exploiting the unrivalled resolution and profiting from the relative simplicity of the experimental implementation.

In recent years, the authors have taught numerous courses on scanning probe microscopy, normally in combination with hands-on student experiments. The audiences ranged from physics freshmen to biology post-docs and even high-school teachers. We found it of particular importance to cover not only the physical principles behind scanning probe microscopy but also questions of instrumental designs, basic features of the different imaging modes, and recurring artifacts. With this book, our intention is to provide a general textbook for all types of classes that address scanning probe microscopy. Third year undergraduates and beyond should be able to use it for self-study or as a textbook to accompany a course on probe microscopy. Furthermore, it will be valuable as a reference book in any scanning probe microscopy laboratory.

The book starts with a thorough introduction, which comprises aspects common to all scanned probe microscopes. These aspects range from the underlying concept of near-field interactions to the construction of mechanical damping systems for the experimental setup. The next three chapters describe in great detail scanning tunneling microscopy, scanning force microscopy, and magnetic force microscopy. In each chapter, a discussion of basic physical concepts is followed by a introduction of experimental procedures, complemented by application examples. For tunneling microscopy, the oldest of these methods, the applications are the focus of its description. The different operation modes are emphasized in the chapter on force microscopy, while the complex interpretation of the results is stressed in the chapter on magnetic force microscopy. The fifth chapter gives brief descriptions of other members of the family of scanning probe microscopes, be the scanning near-field optical microscopy or electrochemical scanning tunneling microscopy. Recurring artifacts in all modes of operation are addressed in Chap. 6. The book closes with a look at the future prospects of scanning probe microscopy, also discussing related techniques in nanoscience.

This book is the outcome of research and teaching at the Department of Physics of the University of Basel, the INM Leibniz-Institute for New Materials (INM) and the Swiss Federal Laboratories for Materials Science and Technology (EMPA). Financial support from the Swiss National Science Foundation (SNF), the Deutsche Forschungsgemeinschaft (DFG), and the Swiss Nanoscience Institute (SNI) is gratefully acknowledged. We also thank the European Research Council (ERC) under the European Unions Horizon 2020 research and innovation programme (ULTRADISS grant agreement No 834402). We would like to acknowledge the contributions of all collaborators, in particular of the mechanical and electronic workshops. We dedicate this book to Hans-Joachim Güntherodt who has been a great tutor and has supported many young scientists in this field. We also acknowledge Alexis Baratoff for his invaluable advice.

Basel, Switzerland

Ernst Meyer  
Roland Bennewitz  
Hans J. Hug

---

# Contents

<b>1</b>	<b>Introduction to Scanning Probe Microscopy</b>	<b>1</b>
1.1	Overview	2
1.2	Basic Concepts	5
1.2.1	Local Probes	6
1.2.2	Scanning and Control	7
1.2.3	Vibrational Isolation	11
1.2.4	Computer Control and Image Processing	12
<b>2</b>	<b>Introduction to Scanning Tunneling Microscopy</b>	<b>13</b>
2.1	Tunneling: A Quantum-Mechanical Effect	14
2.1.1	Tersoff–Hamann Model	16
2.2	Instrumental Aspects	17
2.2.1	Tunneling Tips	17
2.2.2	Implementation in Different Environments	19
2.2.3	Operation Modes	19
2.2.4	Manipulation Modes	23
2.3	Resolution Limits	26
2.3.1	Imaging of Semiconductors	26
2.3.2	Imaging of Metals	26
2.3.3	Imaging of Layered Materials	27
2.3.4	Imaging of Molecules	28
2.3.5	Imaging of Insulators	30
2.3.6	Theoretical Estimates of Resolution Limits	31
2.4	Observation of Confined Electrons	31
2.4.1	Scattering of Surface State Electrons at Steps	32
2.4.2	Scattering of Surface State Electrons at Point Defects	34
2.4.3	Electron Confinement to Nanoscale Boxes	35
2.4.4	Summary of Dispersion Relations for Noble-Metal (111) Surfaces	37
2.4.5	Electron Confinement in Interfacial States of Molecular Layers on Metals	38
2.5	Spin-Polarized Tunneling	38
2.6	Observation of the Kondo Effect and Quantum Mirage	41

2.7	Observation of Majorana Bound States . . . . .	42
2.8	Single-Molecule Inelastic Tunneling Probe . . . . .	43
2.9	Scanning Tunneling Hydrogen Microscopy . . . . .	45
<b>3</b>	<b>Force Microscopy . . . . .</b>	<b>47</b>
3.1	Concept and Instrumental Aspects . . . . .	47
3.1.1	Deflection Sensors: Techniques to Measure Small Cantilever Deflections . . . . .	47
3.1.2	Spring Constants of Rectangular Cantilevers . . . . .	51
3.1.3	Cantilever and Tip Preparation . . . . .	52
3.1.4	Implementations of Force Microscopy . . . . .	53
3.2	Relevant Forces . . . . .	54
3.2.1	Short-Range Forces . . . . .	55
3.2.2	Van der Waals Forces . . . . .	56
3.2.3	Electrostatic Forces . . . . .	57
3.2.4	Magnetic Forces . . . . .	58
3.2.5	Capillary Forces . . . . .	59
3.2.6	Forces in Liquids . . . . .	60
3.3	Operation Modes in Force Microscopy . . . . .	61
3.4	Contact Force Microscopy . . . . .	64
3.4.1	Topographic Imaging . . . . .	64
3.4.2	Lateral Resolution and Contact Area . . . . .	66
3.4.3	Friction Force Microscopy . . . . .	68
3.4.4	Atomic Friction Processes . . . . .	70
3.4.5	Lateral Contact Stiffness . . . . .	73
3.4.6	Velocity Dependence of Atomic Friction . . . . .	74
3.4.7	Temperature Dependence of Atomic Friction . . . . .	75
3.4.8	Molecular Friction . . . . .	77
3.5	Dynamic Force Microscopy . . . . .	78
3.5.1	Modelling Dynamic Force Microscopy . . . . .	80
3.5.2	High-Resolution Imaging . . . . .	82
3.5.3	Spectroscopic Measurements . . . . .	86
3.5.4	Kelvin Probe Microscopy . . . . .	87
3.5.5	Dissipation Force Microscopy . . . . .	89
3.5.6	Non-contact Friction . . . . .	95
3.6	Tapping Mode Force Microscopy . . . . .	95
3.6.1	Principles of Operation . . . . .	95
3.6.2	Phase Imaging . . . . .	96
3.6.3	Non-linear Effects . . . . .	98
3.7	Further Modes of Force Microscopy . . . . .	99
3.8	Pulsed Force Mode . . . . .	100
3.9	Force Resolution and Thermal Noise . . . . .	101

3.10	High-Speed AFM . . . . .	104
3.11	Multifrequency AFM . . . . .	105
<b>4</b>	<b>Magnetic Force Microscopy . . . . .</b>	<b>109</b>
4.1	Principles of Magnetic Force Microscopy . . . . .	109
4.1.1	Early Work . . . . .	109
4.1.2	Tip-Sample Distance Control . . . . .	111
4.1.3	Magnetic Force Microscopy Tips and Cantilevers . . . . .	115
4.2	MFM Contrast Formation . . . . .	119
4.2.1	Negligible Perturbation . . . . .	119
4.2.2	Reversible Perturbation . . . . .	120
4.2.3	Irreversible Perturbation . . . . .	124
4.2.4	Dissipation Contrast . . . . .	127
4.3	Magnetic Stray Fields . . . . .	133
4.3.1	General Concepts . . . . .	133
4.3.2	Field of Thin Film Sample . . . . .	136
4.3.3	Effects of the Domain Wall on the Field . . . . .	139
4.3.4	Fields from Roughness and Thickness Variations . . . . .	140
4.4	Quantitative Magnetic Force Microscopy . . . . .	142
4.4.1	In-Vacuum Operation for Improved Sensitivity . . . . .	143
4.4.2	Tip-Sample Distance Control Suitable for Vacuum . . . . .	147
4.4.3	Separation of Forces . . . . .	156
4.4.4	MFM Transfer Function Theory . . . . .	165
4.4.5	Calibration of the MFM Tip . . . . .	172
4.4.6	Applications of Quantitative MFM . . . . .	176
4.5	Other SPM Methods for Mapping Nanoscale Magnetism . . . . .	194
4.5.1	SPM Methods Mapping the Magnetic Field . . . . .	194
4.5.2	SPM Methods Mapping Magnetism at the Atomic Scale . . . . .	206
<b>5</b>	<b>Other Members of the SPM Family . . . . .</b>	<b>213</b>
5.1	Scanning Near-Field Optical Microscopy (SNOM) . . . . .	215
5.2	Scanning Near-Field Acoustic Microscopy (SNAM) . . . . .	218
5.3	Scanning Ion Conductance Microscopy (SICM) . . . . .	219
5.4	Photoemission Microscopy with Scanning Aperture (PEMSA) . . . . .	220
5.5	STM with Inverse Photoemission (STMiP) . . . . .	221
5.6	Laser Scanning Tunneling Microscopy (LSTM) . . . . .	224
5.7	Electrochemical Scanning Tunneling Microscopy (ECSTM) . . . . .	224
5.8	Scanning Thermal Microscopy (SThM) . . . . .	226
5.9	Scanning Noise Microscopy (SNM) . . . . .	229
5.10	Scanning Tunneling Potentiometry (SPotM) . . . . .	230
5.11	Scanning Capacitance Microscopy (SCM) . . . . .	230
5.12	Scanning Spreading Resistance Microscopy (SSRM) . . . . .	234



5.13	Scanning Tunneling Atom Probe (STAP) . . . . .	238
5.14	Tip Enhanced Raman Scattering (TERS) . . . . .	241
5.15	Photo Induced Force Microscopy (PIFM) . . . . .	241
<b>6</b>	<b>Artifacts in SPM</b> . . . . .	<b>243</b>
6.1	Introduction to Artifacts in SPM . . . . .	243
6.2	Tip Artifact: Convolution with Tip Shape . . . . .	243
6.3	Influence of Local Inhomogenieties on Topography . . . . .	250
6.3.1	STM Topography . . . . .	250
6.3.2	SFM Topography . . . . .	252
6.4	Influence of Topography on Local Measurements . . . . .	253
6.4.1	Influence of Topography on STM-Induced Photon Emission . . . . .	254
6.4.2	Influence of Topography on Lateral Force Measurements . . . . .	255
6.5	Instrumental Artifacts . . . . .	257
6.5.1	Piezoelectric Hysteresis, Creep of Scanners, Nonlinearities and Calibration Errors . . . . .	257
6.5.2	Tip Crashes, Feedback Oscillations, Noise, Thermal Drift . . . . .	259
6.5.3	Interference Patterns with Beam Deflection SFM . . . . .	261
<b>7</b>	<b>Future Aspects of SPM</b> . . . . .	<b>263</b>
7.1	Parallel Operation of SFM Cantilever Arrays . . . . .	263
7.2	Novel Sensors Based on Cantilevers . . . . .	265
7.2.1	Gravimetric Sensors . . . . .	265
7.2.2	Calorimeter Sensors . . . . .	266
7.2.3	Surface Stress Sensors . . . . .	267
7.2.4	Cantilever Array Sensors . . . . .	267
7.3	Molecular Electronics . . . . .	268
7.4	Quantum Computing and Quantum Matter . . . . .	269
7.5	Laboratory on a Tip . . . . .	270
7.6	Local Modification Experiments . . . . .	270
	<b>Bibliography</b> . . . . .	<b>273</b>
	<b>Index</b> . . . . .	<b>319</b>



# Introduction to Scanning Probe Microscopy

# 1

## Abstract

An introduction into the field of scanning probe microscopy is given. These aspects range from the underlying concept of near-field interactions to the construction of mechanical damping systems for the experimental setup.

Richard Feynman foresaw the enormous potential of studying the physics of structures at the nanometer scale in his talk ‘There’s Plenty of Room at the Bottom’ at Caltech in 1959 [178]:

But I am not afraid to consider the final question as to whether, ultimately – in the great future – we can arrange the atoms the way we want; the very atoms, all the way down! What would happen if we could arrange the atoms one by one the way we want them (within reason, of course; you can’t put them so that they are chemically unstable, for example). [...]

What could we do with layered structures with just the right layers? What would the properties of materials be if we could really arrange the atoms the way we want them? They would be very interesting to investigate theoretically. I can’t see exactly what would happen, but I can hardly doubt that when we have some control of the arrangement of things on a small scale we will get an enormously greater range of possible properties that substances can have, and of different things that we can do.

His visionary talk covered a wide range of concepts and opportunities, on which we work today in the field of nanoscience that has since been established. For example, he pointed out the close relationship between physics and biology when it comes to nanostructures and the importance of quantum effects in structures built from a few atoms. His ideas on how to produce nanometer-sized structures included thin-film evaporation through masks, somehow predicting today’s experiments with two-dimensional electron gases. For the construction of few-atom devices, Feynman envisioned a series of machines of decreasing length scale, each generation constructing the next smaller one. This extensive approach has been outrun by a simpler solution: with the invention of scanning probe microscopy, the large gap between the macroscopic world and single-atom manipulation has been bridged in one step.

Near-field interactions between micro-fabricated probes and the sample allow imaging, analysis, and manipulation on the atomic scale, fulfilling Feynman's ideas at least in the laboratory.

This book aims to give an introduction to the field of scanning probe microscopy. Basic concepts are described as well as experimental procedures, with emphasis on scanning tunneling and scanning force microscopy, while other members of this family of methods like scanning near-field optical microscopy are presented in a more general way.

---

## 1.1 Overview

Scanning probe microscopy (SPM) covers a lateral range of imaging from several  $100\text{ }\mu\text{m}$  to  $10\text{ pm}$ . Surfaces of solids can be mapped with atomic resolution, revealing not only the structure of perfect crystalline surfaces but also the distribution of point defects, adsorbates, and structural defects like steps. Scanning probe microscopy has become an essential tool in the emerging field of nanoscience, as local experiments with single atoms or molecules can be performed. Force measurements of single chemical bonds or optical spectra of single molecules may serve as examples. Furthermore, the local probe can be used to manipulate single atoms or molecules and hence to form artificial structures on the atomic scale.

The starting point of SPM was the invention in 1982 of the scanning tunneling microscope (STM) by Binnig and Rohrer [80,85], who were awarded the Nobel prize for physics in 1986. In the STM, a sharp metallic needle is scanned over the surface at a distance of less than  $1\text{ nm}$ . This distance is controlled by the tunneling current between the tip and the conducting surface. The tunneling current is a quantum mechanical effect, with two properties important for STM: it flows between two electrodes even through a thin insulator or a vacuum gap, and it decays on the length scale of one atomic radius. In the STM the tunneling current flows from the very last atom of the tip apex to single atoms at the surface, inherently providing atomic resolution.

In a standard experiment (see Fig. 1.1), the tip is moved in three dimensions by piezoelectric actuators. An electronic controller guides the tip at a tip-sample distance corresponding to a constant preset tunneling current. This distance is recorded by a computer as a function of the lateral position and displayed as a microscope image. High mechanical stability of the experimental setup turns out to be a prerequisite for successful measurements on the atomic scale.

With this example of the STM, all elements of a scanning probe microscope have been introduced. A short-range interaction, yielding the desired resolution, is sensed by a local probe. The probe is scanned over the surface under study, and the measured quantities are recorded and processed in a computer system. The experiment needs a rigid construction and an effective vibrational isolation in order to allow reproducible positioning on the atomic scale.

The family of scanning probe microscopes has several members, based on a variety of tip-sample interactions. The first and most important extension of the STM

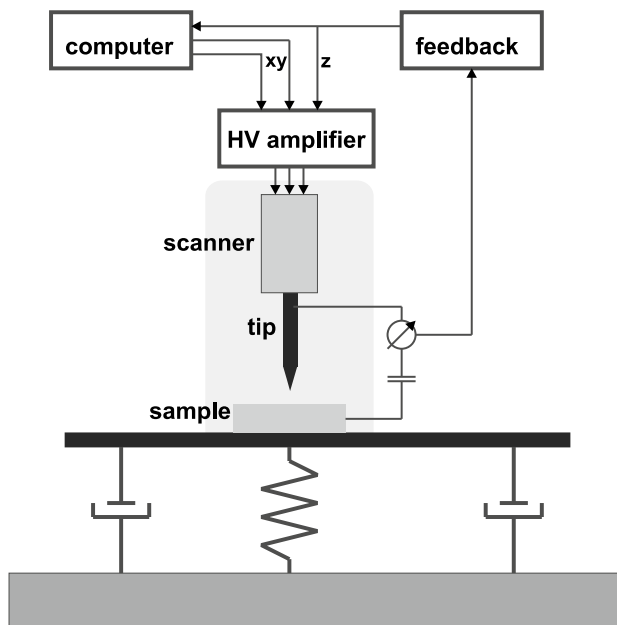


**Fig. 1.1** Basic setup of an STM. The tunneling current is used to control the tip-sample distance  $z$  via a feedback circuit. The distance  $z$  is recorded by a computer as a function of the scanned coordinates  $x$  and  $y$ . A high-voltage amplifier is required to drive the piezoelectric scanner. Good vibrational isolation of the experiment is a prerequisite for high-resolution imaging

was the scanning force microscope (SFM), invented in 1986 by Binnig, Quate, and Gerber [86]. In this instrument, the tip height is controlled in such a way that the force between tip and sample is constant. While the use of the STM is restricted to conducting surfaces, the SFM is in principle capable of determining the topography of any surface, conducting or not. Based on the assumption that forces between the atoms at the tip apex and the atoms of the surface determine the resolution of this instrument, it is commonly called the atomic force microscope (AFM). We will discuss in Chap. 3 the extent to which this assumption is justified. The third distinguished member of the family of SPMs is the scanning near-field optical microscope (SNOM), which uses short-range components of the electromagnetic field as tip-sample interaction.

So far, we have mentioned the imaging capabilities of scanning probe microscopes. Generally, it is said that the movement of the tip at constant tunneling current or constant force reveals the topography of the sample surface. Some caution is required when using the term topography. In STM, it is actually a map of constant density of states that is recorded, and this may differ from the geometric topography. For example, a molecule adsorbed on top of a metal surface may reduce the local density of states and may actually be imaged as a depression. In force microscopy, the situation is even more complicated as different parts of the tip interact differently with features on the surface. The measured height of steps, for example, may deviate significantly from their geometric height. However, on homogenous surfaces

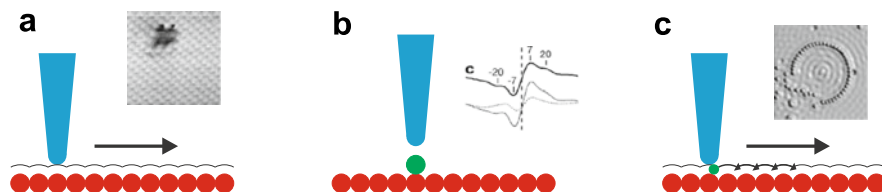


**Fig. 1.2** Different modes of SPM. **a** Imaging the surface with true atomic resolution. **b** Local spectroscopy of surface properties of single molecules on surfaces. **c** Manipulation of surface structure

SPM measurements come as close to the real topography as possible with current experimental methods.

But SPM can do much more than imaging (Fig. 1.2). The electronic structure of the surface can be studied in STM using the so-called spectroscopy modes. Here the tip is stopped at a certain position above the surface and the tunneling current is recorded as a function of the tip–sample voltage. The electronic density of states at different energetic distances to the Fermi level can be derived from such  $I(V)$  curves. Similarly, force versus voltage curves recorded by an SFM reveal the contribution of electrostatic forces and allow the determination of work function differences between tip and sample. Tunneling current and force can also be recorded as a function of the tip–sample distance, and additional information about the tip–sample interactions is obtained. The stability and sensitivity of these spectroscopic methods can be enhanced by employing lock-in techniques. A small oscillating voltage is added to the tip–sample voltage, and its effect on the tunneling current or force is analyzed with a lock-in amplifier. In the same manner, the tip–sample distance can be modulated in order to determine distance dependencies of current or force.

The third important strength of SPM beyond topographic imaging and local measurement of surface properties is the manipulation of surfaces. Single atoms of the surface or adsorbates on it have been systematically moved in STM in order to build nanometer-sized structures. This can be accomplished by pushing or pulling the atoms with the tip, or even by transfer of atoms to and from the tip. Such experiments establish a lithography on the molecular scale. STM is not the only tool for surface manipulation. The tip of an SFM can be used to deposit charges on insulating samples, or to study microscopic effects in wear by scratching the surface. Single molecules can be optically bleached by a SNOM. All these examples share the fact that the results and effects of manipulation are studied with the same tip that was used as a tool to perform it.

Scanning probe microscopy has found wide applications in Surface Science, where problems like surface structure, adsorption of molecules, or local electronic properties could be studied. The first nanostructures have been built in an atom-by-atom way and characterized. More industrial applications include surface control in Materials Science. Roughness and hardness are being measured on the nanometer scale. Magnetic structures on data storage devices can be analyzed as well as the optical quality of coatings. The microscopic origins of friction have been investigated by SFM. Force microscopy allows nanometer-scale imaging of biological materials

# Introduction to Scanning Tunneling Microscopy

# 2

## Abstract

An introduction is given into scanning tunneling microscopy (STM), where a small tunneling current is measured between probing tip and sample. Various operation modes, such as constant tunneling and constant height modes as well as tunneling spectroscopy, are described and application examples are given.

Scanning tunneling microscopy (STM) was invented by Binnig and Rohrer (see Fig. 2.1) [80, 109]. Using the combination of a coarse approach and piezoelectric transducers, a sharp, metallic probing tip is brought into close proximity with the sample. The distance between tip and sample is only a few angstrom units, which means that the electron wave functions of tip and sample start to overlap. A bias voltage between tip and sample causes electrons to tunnel through the barrier. The tunneling current is in the range of pA to nA and is measured with a preamplifier.<sup>1</sup> This signal is the input signal of the feedback loop, which is designed to keep the tunneling current constant during  $(x, y)$ -scanning. The output signal is amplified (high voltage amplifier) and connected to the  $z$ -piezo. According to the feedback output voltage and the sensitivity of the piezo (typically nm/V) the tunneling tip is moved backwards or forwards and the tunneling current is kept constant during acquisition of the image. This operation mode is called constant current mode.

There exist other modes, such as the constant height mode, where the tip is moved at constant height and variations in the current are measured. The  $(x, y)$ -movement of the tip is controlled by a computer. The  $z$ -position (output of feedback loop) is measured at discrete  $(x, y)$ -positions. The data  $z(x_i, y_j)$  can be displayed in several

<sup>1</sup> $I$ – $V$  converters are used to convert the tunneling current into a voltage. A possible realisation consists of an operational amplifier (e.g., Burr Brown OPA 111) and a resistor  $R$ , where the output voltage is given by  $V_{\text{out}} = RI$ . With a resistor of the order of  $R = 100 \text{ M}\Omega - 1 \text{ G}\Omega$ , currents of the order of nanoamperes,  $I_t \approx 1 \text{ nA}$ , are measurable. Smaller currents of the order of  $0.1 \text{ pA}$  are more difficult to measure. Field-effect transistors are needed very close to the tip.

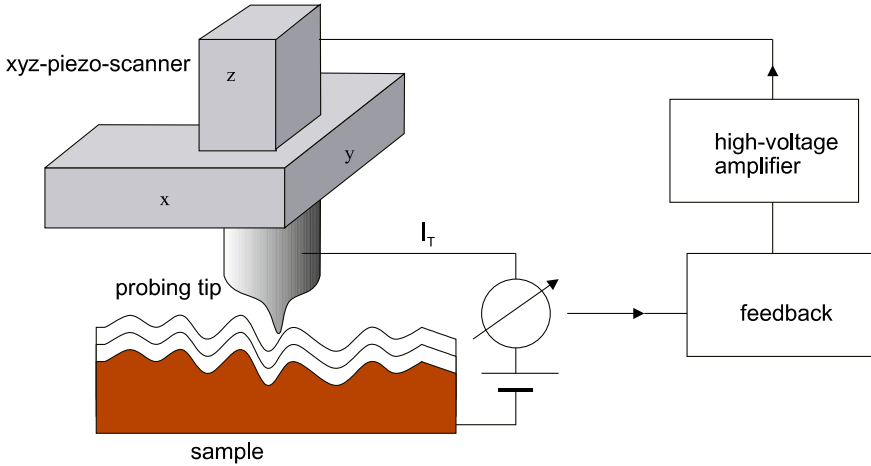


**Fig. 2.1** Schematic diagram of the scanning tunneling microscope. An  $xyz$ -piezoelectric scanner moves the tip over the surface. A feedback loop can be used to keep the tunneling current constant

ways: line-scan image, grey-scale image or colour encoded image.<sup>2</sup> The line-scan image is the most natural way to represent the data, because each line represents the scan of the tip in the fast direction. However, grey-scale images or colour encoded images are more frequently used, because they are better adapted to human pattern recognition. Bright spots represent hillocks or protrusions and dark spots represent valleys or depressions.

Scan areas are limited by the choice of the piezoelectric scanner and the maximum output voltage  $V_{\max}$  of the high voltage amplifier. With a typical sensitivity of 3 nm/V and  $V_{\max} = 250$  V, a maximum scan range of 750 nm can be achieved. Some commercial scanners are designed for ranges of up to 100  $\mu\text{m}$ . However, these large scanners are often inadequate for atomic-scale imaging. Thus, the maximum scan range of high resolution STMs is in the range 1000 nm = 1  $\mu\text{m}$ . Whether the microscope can achieve atomic resolution depends on the stability of the instrument and the vibrational isolation. In Chap. 1 the design of these components is explained in more detail. Generally, the mechanical construction of the STM should be rigid with a high resonance frequency ( $\approx 1$  kHz) and the vibrational isolation should have a low resonance frequency ( $\approx 1$  Hz) with low  $Q$ -factor ( $Q \approx 1$ ).

## 2.1 Tunneling: A Quantum-Mechanical Effect

According to quantum mechanics, a particle with energy  $E$  can penetrate a barrier  $\phi > E$  (see Fig. 2.2). In the classically forbidden region, the wave function  $\psi$  decays

<sup>2</sup>Selection of the number of data points is user-defined, e.g.,  $400 \times 400$ ,  $500 \times 500$  or  $1000 \times 1000$ . If fast fourier algorithms are to be used, powers of two,  $2^N$ , are favourable, e.g.,  $256 \times 256$ ,  $512 \times 512$  or  $1024 \times 1024$ .

## Abstract

An introduction is given into atomic force microscopy (AFM), where a force is detected between probing tip and sample. Force detections schemes as well as operation modes are discussed. Various force interactions can be distinguished, such as repulsive contact forces, chemical forces, electrostatic forces or magnetic forces. Application examples will be shown for the various sample categories ranging from metals to insulators.

## 3.1 Concept and Instrumental Aspects

The basic concept of force microscopy is the measurement of forces between a sharp tip and a sample surface. Most commonly, the tip is mounted on the end of a cantilever which serves as a force sensor. Either the static deflection of the cantilever or the change in its dynamic properties due to tip-sample forces can be exploited. The limit of force detection is far lower than the force between atoms at lattice distances, explaining the widely used term atomic force microscope. In analogy to scanning tunneling microscopy, we will refer to the method as scanning force microscopy (SFM).

### 3.1.1 Deflection Sensors: Techniques to Measure Small Cantilever Deflections

There are different techniques to detect the small bending of the cantilever due to tip-sample forces (see Fig. 3.1). Most instruments use the beam-deflection method [24, 432, 453]. A light beam is reflected at the rear side of the cantilever and the deflection is monitored by a position-sensitive photodiode. A schematic drawing of the setup is shown in Fig. 3.2. A four-segment photodiode allows one to detect not



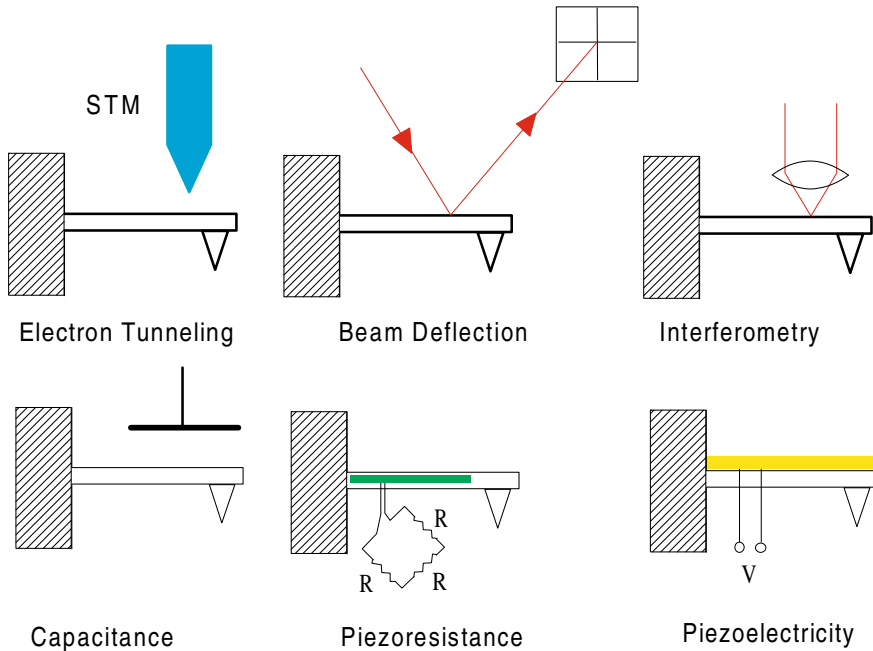


**Fig. 3.1** Deflection sensors for scanning force microscopy

only the normal bending, but also the torsion of the cantilever caused by lateral forces acting on the tip.

An alternative deflection sensor can be implemented by using the cantilever as one mirror of an optical laser interferometer [560]. This technique has the advantage of easy calibration by the wavelength of the light. Furthermore, it can be implemented if space is limited, as in low-temperature experiments. Both optical methods have achieved a sensitivity which is limited by the thermal noise of the cantilever. An intriguingly simple version of an interferometer has been presented by Sarid et al., where the reflected light from the cantilever is fed back into the laser diode cavity [573].

The cantilever deflection can also be detected by a change in the capacitance between the cantilever and a counterelectrode [443]. This technique is capable of a very fast measurement, and the whole force sensor can be produced by microfabrication techniques [88]. A drawback with this sensor is the force between cantilever and counterelectrode, which cannot be neglected. On the other hand, the electrostatic force can also be used to control the deflection in a force feedback scheme [168]. In the original force microscope of Binnig et al., the cantilever deflection was detected by means of a tunneling current from the cantilever to an STM tip positioned at the rear side of the cantilever [86]. This otherwise very sensitive setup is also complicated by the force between the STM tip and the cantilever.

Self-sensing cantilevers form a very elegant class of deflection sensors. Most are realized by producing a piezoresistive layer on a silicon cantilever [650]. Although

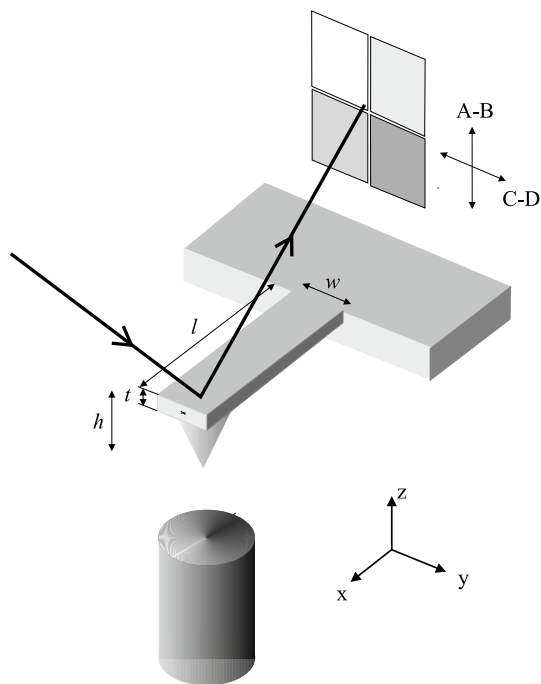


**Fig. 3.2** Schematic diagram of the beam-deflection SFM. The relevant dimensions of the rectangular cantilever are indicated: length  $l$ , width  $w$ , thickness  $t$  and height of the tip  $h$ . Note that  $h = h_{\text{tip}} + t/2$ . Normal and lateral forces acting on the tip are measured via normal and torsional motions of the cantilever. A light beam is reflected off the rear side of the cantilever. Angular deflections of the laser beam are measured with a position-sensitive detector (4-quadrant photodiode). The A-B signal is proportional to the normal force and the C-D signal is proportional to the torsional force

the signal-to-noise ratio is comparable to beam-deflection schemes, the first dynamic measurement showing atomic resolution was performed with piezoresistive cantilevers [203]. Other dedicated designs allow the piezoresistive detection of lateral forces [119,225]. Piezoelectric cantilevers have the advantage of being sensor and actuator for dynamic measurements at the same time. This ability has been exploited in the compact design of a high-vacuum dynamic force microscope [118] and for a significant enhancement of the speed of tapping mode force microscopy [630]. Commercially available quartz tuning forks are cheap piezoelectric sensors with high frequency and spring constant. High-resolution images in dynamic mode have been achieved by attaching sharp probing tips to such quartz tuning forks [123,205,209,210]. The setup is ideal for low temperatures in combination with STM. In this case, a tungsten wire is attached to one the prongs and the second prong is fixed, also called Q-Plus setup [210]. It is also found that the Q-factors at low temperatures can reach 30'000–50'000, which gives excellent force (gradient) sensitivity. Under these conditions submolecular resolution was achieved on planar molecules [231] (Fig. 3.3).

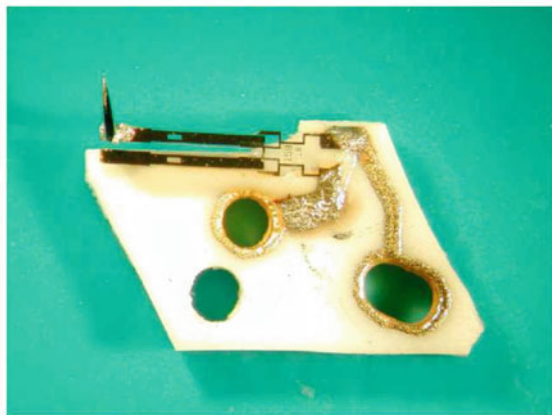


**Fig. 3.3** Photograph from a tuning fork AFM. One of the prongs is fixed, also called Q-Plus [210]. The probing tip is glued to the other prong. Typical spring constant is 1800 N/m. Oscillation amplitudes of 10–100 pm can be selected. Especially, at low temperatures the internal damping is very low and Q-factor of 30'000–50'000 are measured. Therefore, excellent force sensitivity can be achieved. Reprinted from [210], <https://link.aps.org/doi/10.1103/RevModPhys.75.949>, with permission from AIP Publishing

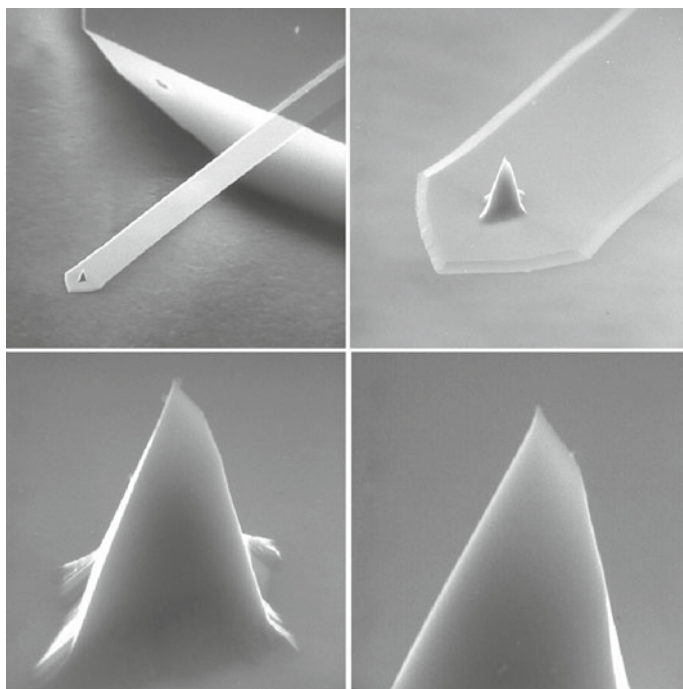


**Fig. 3.4** Scanning electron microscopy images of a rectangular silicon cantilever with integrated probing tip, manufactured by Nanosensors. The height of the probing tip is 12.5  $\mu\text{m}$  [10]



## Abstract

This chapter is related to the field of magnetic force microscopy (MFM), where the probing tip is covered with a magnetic layer and the magnetic domain structure of the sample can be characterized with high lateral resolution. In addition, other scanning probe methods mapping the magnetic field at a microscopic scale and techniques providing access to atomic scale magnetism are reviewed.

## 4.1 Principles of Magnetic Force Microscopy

### 4.1.1 Early Work

Magnetic Force Microscopy is a versatile technique used to map the stray field emanating from a sample surface with high spatial resolution and sensitivity. The magnetic force microscope (MFM) is an atomic (or scanning) force microscope [86] with a tip that is made sensitive to magnetic stray fields. First results by Martin and Wickramasinghe [433], Abraham et al. [15], and Mamin et al. [423] demonstrated a lateral resolution of about 100 nm on thin film magnetic recording heads and magnetization patterns in longitudinal recording media. Cantilevers were fabricated by etching iron and nickel wires and bending these into an L-shape. These cantilevers were oscillated at a fixed frequency near their fundamental mode resonance frequency. The tip-sample interaction arising from the sum of the van der Waals, electrostatic and magnetic force gradients then shifts the cantilever resonance frequency, and leads to a corresponding change of the cantilever oscillation amplitude or phase between the cantilever oscillation and drive signals. These signals were measured by a lock-in amplifier and the amplitude was used for the tip-sample distance feedback [Fig. 4.1a]. Depending on the reaction speed of the z-feedback loop, the oscillation amplitude signal can be kept constant locally or on average. The local force gradient acting on the cantilever is then reflected by the change of the z-position [out B in Fig. 4.1a] or the change of the cantilever oscillation amplitude [out A in Fig. 4.1a [423]]. Mamin

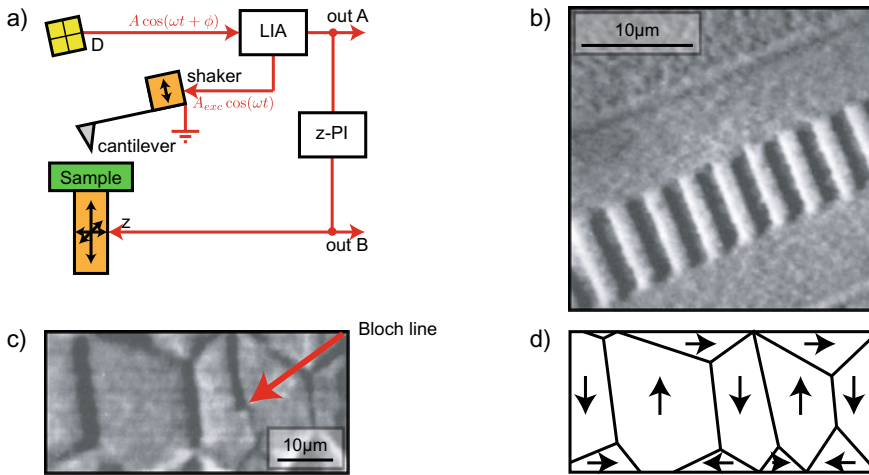


**Fig. 4.1** **a** Block of the electronic circuitry of the MFM operated in the dynamic mode. The cantilever is driven near its resonance. **b** MFM image of an 8  $\mu\text{m}$  wide track written in a CoPtCr media with in-plane magnetic anisotropy (adapted from [561], with permission from AIP Publishing). **c** MFM image of a permalloy thin film. The domain walls are visible either as dark or bright lines. The red arrow points a Bloch line (adapted from [424], <https://doi.org/10.1063/1.101898>, with permission from AIP Publishing)

et al. already pointed out several aspects that remained of high relevance also for current MFM work. First, accurate tip-sample distance control is required and a higher lateral resolution can be obtained if the tip is scanned at a small tip-sample distance. Second, the differentiation between the contrast arising from the topography of the sample and that from the magnetic tip-sample interaction can be challenging.

It is noteworthy that at a time where all atomic force microscopes used for topographical imaging were operated in static modes, dynamic scanning force microscopy operation modes were used in all of the early work of the IBM [423, 424, 433, 435] and Philips [141] research groups. With the latter operation modes, reliable non-contact imaging was possible, and reproducible MFM results of stray fields of recording heads [433], written bits in recording materials [141, 435, 561] [Fig. 4.1b], permalloy elements [424] [Fig. 4.1c and d] and natural domains [141] in CoPt multilayers were obtained.

Other early work either scanned the tip in contact with the sample [235, 568] or used tunneling between the tip and sample [221] to control the tip-sample distance. Under such operation conditions large non-magnetic forces act on the tip. The force constant relevant for the magnetic tip-sample interaction then becomes

$$c_{\text{eff}} = c_L - \frac{\partial F_{\text{nm}}}{\partial z}, \quad (4.1)$$

where  $c_L$  is the force constant of the cantilever and  $\frac{\partial F_{\text{nm}}}{\partial z}$  is the  $z$ -derivative of the non-magnetic forces. Typically  $|c_{\text{eff}}| \gg c_L$ . Hence, the deflection of the cantilever [235, 568] or change of its resonance frequency arising from the magnetic forces

## 4.3 Magnetic Stray Fields

### 4.3.1 General Concepts

It is convenient to introduce the concept of magnetic charges to calculate the magnetic stray field  $\mathbf{H}$  emanating from a magnetization pattern  $\mathbf{M}$  inside a sample and to understand which information on the latter can be deduced from measurements of the former. Magnetic charges can be defined from one of Maxwell's equations as

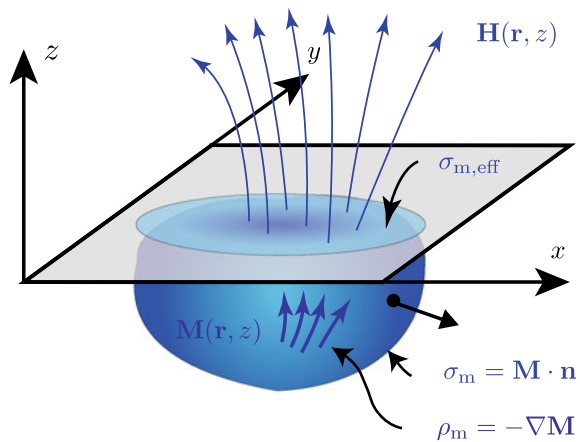
$$\nabla \mathbf{B} = \mu_0 \nabla (\mathbf{H} + \mathbf{M}) = 0 \Rightarrow \nabla \mathbf{H} = -\nabla \mathbf{M}, \quad (4.11)$$

where  $\rho_m := -\nabla \mathbf{M}$  is the magnetic volume charge arising from a divergence of  $\mathbf{M}$  inside a magnetic sample. In addition, magnetic surface charges  $\sigma_m := \mathbf{n} \cdot \mathbf{M}$  occur at the surfaces of a magnetic sample if there is a magnetization component parallel to the normal vector  $\mathbf{n}$  of the sample [Fig. 4.18]. The magnetic stray field emanating from the surface of a sample can then be written analogous to the electric field arising from electric charges [308] as

$$\mathbf{H} = \int_V \nabla \mathbf{M}(\mathbf{x}') \frac{\mathbf{x} - \mathbf{x}'}{|\mathbf{x} - \mathbf{x}'|^3} d^3 \mathbf{x}' + \int_A \mathbf{n} \cdot \mathbf{M} \frac{\mathbf{x} - \mathbf{x}'}{|\mathbf{x} - \mathbf{x}'|^3} d^2 \mathbf{x}', \quad (4.12)$$

where the first and second integrals arise from the magnetic volume,  $\rho_m$ , and magnetic surface charges,  $\sigma_m$ , respectively. Because the magnetization (as any vector field bounded in the domain  $V \subseteq \mathbb{R}^3$  which is twice continuously differentiable) can be decomposed as  $\mathbf{M} = \mathbf{M}_{\text{irr}} + \mathbf{M}_{\text{div}}$ , where  $\nabla \times \mathbf{M}_{\text{irr}} = 0$  is a curl-free and  $\nabla \cdot \mathbf{M}_{\text{div}} = 0$  is a source-free component. It is obvious that the latter component does not contribute to the sample stray field and is thus not accessible by MFM. Moreover, for all spatial distributions of the magnetic volume charge  $\rho_m$  inside a magnetic sample and magnetic surface charge  $\sigma$  on its boundaries, an effective magnetic surface charge  $\sigma_{m,\text{eff}}$  generating the same magnetic stray field exists (see (4.44) in

**Fig. 4.18** The stray field,  $\mathbf{H}(\mathbf{r}, z)$  arises from the magnetic volume charge density,  $\rho_m(\mathbf{r}, z) = -\nabla \mathbf{M}(\mathbf{r}, z)$  and from the magnetic surface charge density,  $\sigma_m = \mathbf{M}(\mathbf{r}, z) \cdot \mathbf{n}(\mathbf{r}, z)$



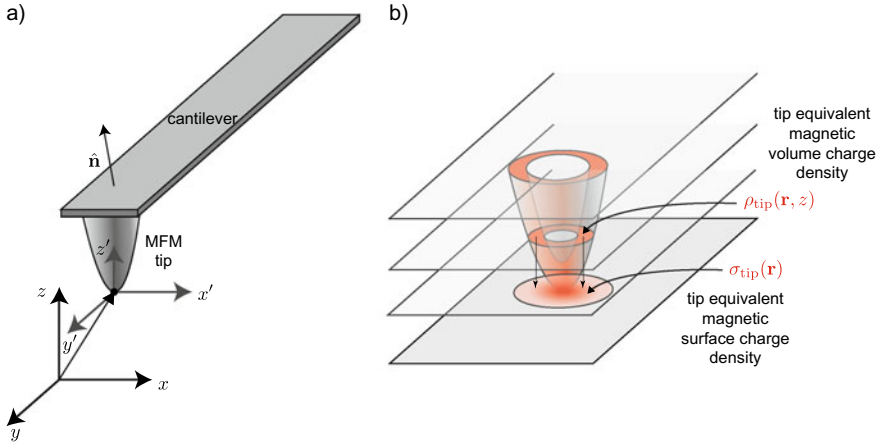


**Fig. 4.36** **a** Coordinate systems and cantilever with normal vector  $\hat{n}$  canted towards the surface. **b** Magnetic charge distribution of the tip,  $\rho_{\text{tip}}$ , and its propagation to an xy-plane running through the tip apex with the tip equivalent magnetic surface charge density  $\sigma_{\text{tip}}$  that fully characterizes the magnetic imaging properties of the tip

The magnetostatic force acting on the tip given by (4.75) then becomes

$$\mathbf{F}(\mathbf{r}, z) = \mu_0 \int [\mathbf{M}(\mathbf{r}', z') \cdot \nabla] \mathbf{H}(\mathbf{r} + \mathbf{r}', z + z') d\mathbf{r}' dz', \quad (4.77)$$

and in the two dimensional Fourier space already used to conveniently calculate stray fields (Sect. 4.3) the force is given by

$$\mathbf{F}(\mathbf{k}, z) = \mu_0 \int [\mathbf{M}(\mathbf{r}', z') \cdot \nabla] \left[ \int \mathbf{H}(\mathbf{r} + \mathbf{r}', z + z') e^{-i\mathbf{k}\mathbf{r}} d\mathbf{r} \right] d\mathbf{r}' dz'. \quad (4.78)$$

Using the coordinate transformations  $\tilde{\mathbf{r}} := \mathbf{r} + \mathbf{r}'$  and  $d\tilde{\mathbf{r}} = d\mathbf{r}$ , (4.78) can be re-written as

$$\begin{aligned} \mathbf{F}(\mathbf{k}, z) &= \mu_0 \int [\mathbf{M}(\mathbf{r}', z') e^{i\mathbf{k}\mathbf{r}'} \cdot \nabla] \underbrace{\int \mathbf{H}(\tilde{\mathbf{r}}, z + z') e^{-i\mathbf{k}\tilde{\mathbf{r}}} d\tilde{\mathbf{r}}}_{= \mathbf{H}(\mathbf{k}, z + z')} d\mathbf{r}' dz' \\ &= \mu_0 \cdot \mathbf{H}(\mathbf{k}, z) \int \underbrace{\int \mathbf{M}(\mathbf{r}', z') e^{i\mathbf{k}\mathbf{r}'} d\mathbf{r}'}_{= \mathbf{M}^*(\mathbf{k}, z')} e^{-kz'} dz' \cdot \begin{pmatrix} ik_x \\ ik_y \\ -k \end{pmatrix} \\ &= \mu_0 \cdot \mathbf{H}(\mathbf{k}, z) \int \rho_{\text{tip}}^*(\mathbf{k}, z') e^{-kz'} dz' \\ &= \mu_0 \sigma_{\text{tip}}^*(\mathbf{k}) \cdot \mathbf{H}(\mathbf{k}, z), \end{aligned} \quad (4.79)$$

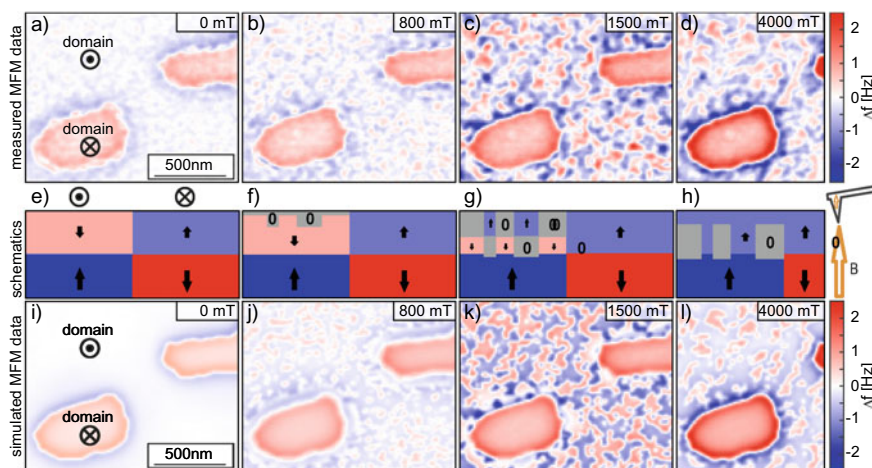


**Fig. 4.46** **a** to **d** MFM images measured in fields of 0–4000 mT on an exchange coupled ferro/ferrimagnet double layer, Pt(3)/[Pt(0.7)/Co(0.4)]<sub>×5</sub>/Tb<sub>26.5</sub>Fe<sub>73.5</sub>(20)/Pt(10)/SiO<sub>2</sub>/Si sample. **e** to **h** Schematics of candidate magnetization structures used for modeling the MFM contrast of the different magnetization stages. **i** to **l** Modeled MFM images obtained from the candidate magnetization structures (see Zhao et al. [729] for details). Figure adapted from Zhao et al. [729] with permission from American Chemical Society

or the misalignment of the grains' easy axis with the z-direction which are both not considered in the candidate magnetization structure.

In stage 1, the gradual increase of the contrast is compatible with a rotation of the initially down magnetic moments of Co/Pt toward the field (up) direction. Because the magnetic moments of the Co/Pt multilayer at the interface are pinned to the magnetic moments of the high-anisotropy TbFe film, the Co/Pt multilayer magnetic moments at the top surface are expected to rotate more than those near the interface. For the modeling of the MFM contrast, the vertical structure of the spin chains at any given location on the image plane is modeled by a corresponding spatial distribution of “subdomain blocks” with zero magnetization, located at the top of the Co/Pt multilayer and reaching into different depths toward the interface [gray blocks in Fig. 4.46f]. The lateral distribution of these blocks can be inferred from the granular contrast observed in the MFM  $\Delta f(\mathbf{r}, z_{ts})$ -data displayed in Fig. 4.46b. With optimized sublayer depths, again an excellent agreement between the modeled and measured MFM  $\Delta f(\mathbf{r}, z_{ts})$ -data could be obtained [compare, for example, Fig. 4.46k–c].

In stage 2, a strong increase of the contrast is accompanied by a substantial change in the appearance of the granular pattern. These observations are compatible with isolated Co/Pt grains switching their magnetization from a canted down to a canted up state (as was used in the modeling). This is reminiscent of a Stoner–Wohlfarth magnetization process with a field applied away from the easy axis where an instability of the magnetization state occurs. The candidate magnetization structure for stage 2 is depicted in Fig. 4.46f. With the latter, again an excellent agreement of the



ments working under ambient conditions. Section 4.4.1 describes the advantages of operating a magnetic force microscope in vacuum discussing the improved signal-to-noise ratio possible with cantilevers reaching quality factors between 200'000 and 1'000'000. The operation in vacuum requires the use of more advanced tip-sample distance control modes described in Sect. 4.4.2. These operation modes, however allow the use of cantilevers with a stiffness around 0.3 N/m which is typically 10 times softer but have about the same resonance frequency as the cantilevers used for intermittent-contact/lift-mode operation (see Sect. 4.1.2) in the work of Hu et al. [290]. Consequently, according to (4.50), the sensitivity of the MFM operated with the high-quality factor cantilever in vacuum compared to the instruments used in the work of Hu et al. [290] is about 100–200 times better.

This demonstrates the advantages MFM operated with highest quality factor cantilevers using advanced operation modes, but also the necessity for commercially available instruments that can be operated under such conditions to make quantitative magnetic force microscopy methods accessible to more groups and thus to more widely explore the full potential of such experimental methods for the analysis of magnetic materials.

---

## 4.5 Other SPM Methods for Mapping Nanoscale Magnetism

### 4.5.1 SPM Methods Mapping the Magnetic Field

Various scanning probe methods used to map nanoscale magnetism have been developed. Here, only methods that have been widely applied by different groups to study various materials are reviewed. For this reason, spin-polarized tunneling scanning tunneling microscopy (SP-STM) and exchange force microscopy (MExFM) are discussed in Sects. 4.5.2.1 and 4.5.2.2, while other STM-based techniques that can address atomic scale magnetism like spin-flip tunneling [268,278,346] and single atom magnetic resonance imaging [699] are not described here.

MFM is a robust lab tool to image stray fields emanating from magnetic sample surfaces with high spatial resolution at various temperatures and in fields of up to several Tesla and can even perform quantitative field measurements. However, the ferromagnetic tip used in MFM inevitably generates a stray field that can perturb the micromagnetic state of the sample (see Sects. 4.2.2 and 4.2.3), particularly if magnetically-soft samples are imaged with large magnetic moment tips (which are often used to compensate, for example, for the lack of sensitivity if an MFM is operated under ambient conditions). Further, the MFM tip is a finite-size nanoscale object, inherently limiting the lateral resolution to about 10 nm [446]. In order to overcome these limitations of the MFM, other scanning probe techniques sensitive to the magnetic stray field that are less invasive, including one with an atomic-scale field sensor, have been developed. All methods mapping the stray field have in common the fact that from the measured stray field only limited information on the magnetization distribution inside the sample can be obtained. This is because the stray field emanates from magnetic surface and volume charges (see Sect. 4.3.1) arising

from the divergence of the magnetization field. Different magnetization fields can have the same divergence and, trivially, any divergence-free magnetization field does not generate a stray field. Furthermore, because the stray field outside a magnetic sample is a conservative field, i.e. is generated from a scalar potential, all vector components of the stray field can be calculated from a single component of the stray field measured in a plane above a sample (see (4.26) and Fig. 4.53). The stray field decays exponentially into the outside space with a decay constant given by the spatial wavelength of the stray field. It is hence advantageous to maximize the sensitivity of the field sensor, and to scan it at the smallest possible tip-sample distance. While for MFM substantial efforts have been undertaken to obtain a robust tip-sample distance control (see Sects. 4.1.2 and 4.4.2), corresponding experimental techniques have unfortunately not yet been explored extensively for other SPM methods mapping the stray field.

#### 4.5.1.1 Scanning Hall Probe Microscopy

Scanning Hall probe microscopy [103, 501] is often described as a non-invasive (the magnetic field generated by the Hall sensor current can be neglected) and quantitative technique to map stray field emanating from the sample surface. While the first is correct, the latter statement can not be made for fields varying over the spatial wavelengths of the same order or smaller than the size of the Hall bar structure. Then, the part of the stray field component perpendicular to the Hall bar sensor passing through it must be assessed before a quantitative analysis of the stray field at the surface of the sample can be performed. Further, a quantitative mapping of the stray field can only be compared to that calculated from model-magnetization structures, if the distance between the Hall sensor and the surface of the sample has been determined.

First SHPM data with sub-micron spatial resolution were demonstrated by Chang et al. [103]. A submicron Hall structure fabricated from a GaAs/Al<sub>0.3</sub>Ga<sub>0.7</sub>As heterostructure was used to obtain a spatial resolution of about 0.35  $\mu\text{m}$  and a field sensitivity of about 0.01 mT. The Hall bar was structured close to the edge of a chip, and the chip edge was used as a tunneling tip to control the distance between the Hall bar structure and the surface [Fig. 4.56a]. Images of vortices in a c-axis oriented La<sub>1.85</sub>Sr<sub>0.15</sub>CuO<sub>4</sub> of 0.8  $\mu\text{m}$  thickness are displayed in Fig. 4.56b and c. Vortices in a 350 nm-thick YBa<sub>2</sub>Cu<sub>3</sub>O<sub>7- $\delta$</sub>  film on MgO [Fig. 4.56d] were later imaged by Oral et al. [501] also using a GaAs/Al<sub>0.3</sub>Ga<sub>0.7</sub> as Hall bar, albeit with a slightly larger dimension (Hall bar wire width of 1  $\mu\text{m}$ ).

In principle, a smaller Hall bar structure would be beneficial for the spatial resolution. The minimum size of the GaAs/Al<sub>0.3</sub>Ga<sub>0.7</sub> is however limited to about 1.5  $\mu\text{m}^2$  because of surface depletion effects of the 2D electron gas. Much smaller Hall bar structures could be fabricated using single crystalline InSb [Fig. 4.57a] and polycrystalline Bi [Fig. 4.57c]. A field sensitivity of about 0.08 mT/ $\sqrt{\text{Hz}}$  was obtained. However, the Hall bar cross is about 5–10  $\mu\text{m}$  away from the metal edge used as a tunneling tip for distance control [see arrow in Fig. 4.57a] such that the distance between the Hall bar and the sample surface is about 80 nm for a tilt angle of 1.2°

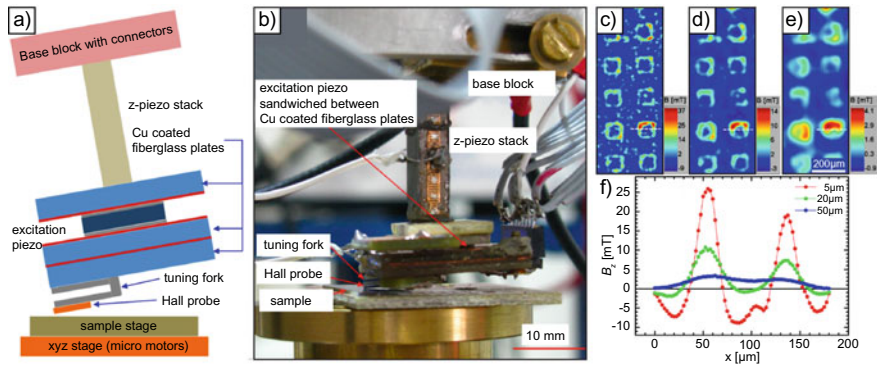


**Fig. 4.58** **a** Schematics of the microscope. **b** Optical image of the microscope showing the probe and sample stages. **c**, **d**, and **e** SHPM images of the  $B_z$  distribution above a printed structure consisting of  $100\ \mu\text{m} \times 100\ \mu\text{m}$  squares of NdFeB powder acquired at a Hall probe to surface distance of 5, 20, and  $50\ \mu\text{m}$ , respectively. **f** Corresponding cross-sections of the  $B_z$  distributions. Figure adapted from Shaw et al. [600] with permission from AIP Publishing

d and e show SHPM images of hard magnetic powder (NdFeB) based micro-flux sources acquired at 5, 20, and  $50\ \mu\text{m}$  Hall probe to sample distance.

Imaging stray fields at wavelengths considerably larger than the Hall probe sensor size also permits quantitative field measurements. The traceability of calibrated Hall probes fabricated close to the tip of AFM cantilevers has recently been investigated by Gerken et al. [202]. This work also reviews different materials for the Hall sensors and points out under which conditions these are best used.

#### 4.5.1.2 Scanning SQUID Microscopy

A superconducting quantum interference device (SQUID) is a superconducting ring typically containing two weak links, each having the same critical (super) current  $I_0$  for the case of a symmetrical SQUID [Fig. 4.59a]. The critical current through the SQUID (through both weak links) then becomes periodic in the applied magnetic flux  $\phi_a$  with a period given by the flux quantum  $\phi_0 \approx 2.067 \cdot 10^{-15}$  Wb. If an applied current is biased just above the critical current [Fig. 4.59b], the voltage drop across the SQUID varies sinusoidally [Fig. 4.59c]. In order to determine the magnetic flux penetrating the SQUID, typically a flux-closed loop with an ac-flux modulation scheme is applied [121, 351]. A feedback then applies a flux  $\delta\phi$  to the SQUID loop such that the dc component of the total flux (external flux  $\phi_a$  from the applied magnetic field and flux  $\delta\phi$  generated by the feedback) is set such that the SQUID voltage is at an extremum, and the first harmonic arising from the flux modulation vanishes [Fig. 4.59d]. For microscopy the SQUID loop or a pick-up loop integrated into the SQUID must be made small and brought close to the surface of the sample [351]. The first two-dimensional scanning SQUID microscope was built by Rogers and Berman at IBM research [554] to image superconducting vortices in devices designed for the IBM Josephson computer program. As reviewed by Kirtley [351], there are different competing strategies for improving the spatial resolution of a

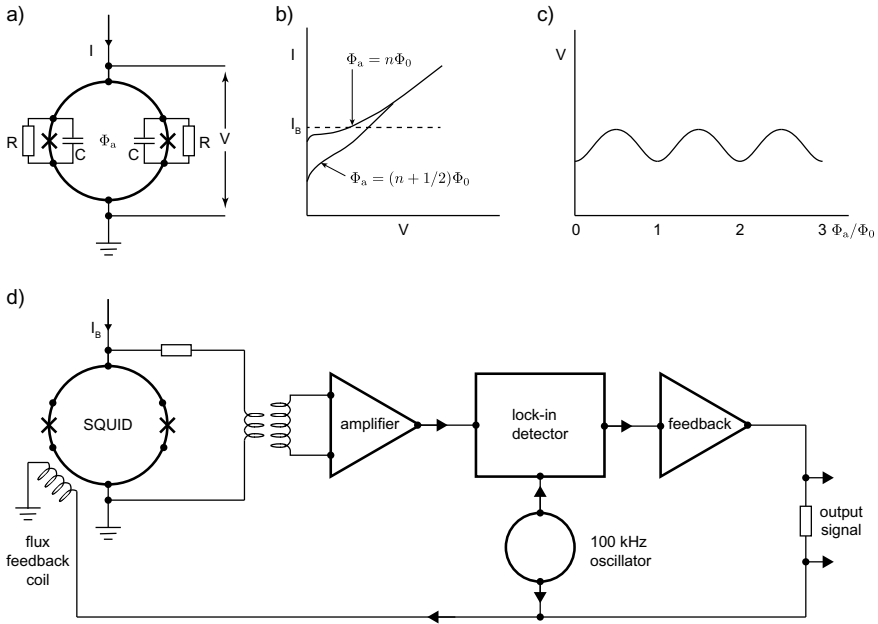


**Fig. 4.59** **a** Schematics of a dc SQUID with two identical weak links (crosses). **b**  $I$ - $V$ -characteristics. **c**  $V$  versus  $\phi_a/\phi_0$  at constant bias current  $I_B$ .  $\phi_0 \approx 2.067 \cdot 10^{-15}$  Wb is the flux quantum. **d** Schematics of the flux-closed loop. Figure adapted from Clarke et al. [121]

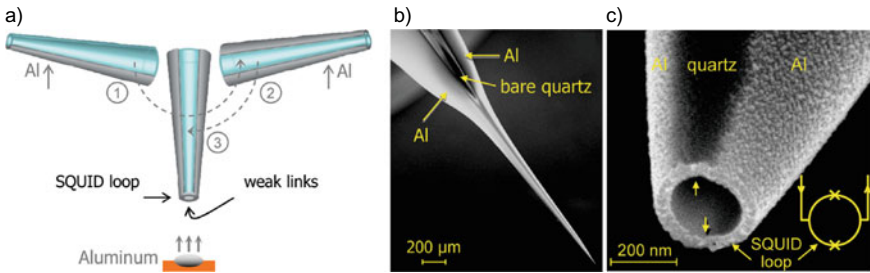


**Fig. 4.60** **a** Schematic description of three self-aligned deposition steps for fabrication of SOT on a hollow quartz tube pulled to a sharp tip (not to scale). In the first two steps, aluminum is evaporated onto opposite sides of the tube forming two superconducting leads that are visible as bright regions separated by a bare quartz gap of darker color in the SEM image (**b**). In a third evaporation step, Al is evaporated onto the apex ring that forms the nanoSQUID loop shown in the SEM image (**c**). The two regions of the ring between the leads, marked by the arrows in (**c**), form weak links acting as two Josephson junctions in the SQUID loop. The schematic electrical circuit of the SQUID is shown in the inset of (**c**). Figure adapted from Finkler et al. [180] with permission from American Chemical Society

SQUID microscope sensor: First, the SQUID loop can be fabricated very small with narrow and thin constructions of the Josephson weak links. Hao et al. [256] reported a SQUID sensor with a diameter of about  $370 \text{ nm}$  and a noise level of  $0.2 \mu\phi_0/\sqrt{\text{Hz}}$ .

### 4.5.1.3 NV Center Microscopy

To improve the lateral resolution of microscopes mapping the magnetic field, Chernobrod and Bergman [113], based on earlier ideas of Sekatskii and Letokov [596], proposed the use of single spin nanoscale quantum sensors. The main advantages are that the sensor has atomic scale dimensions and can offer excellent field sensitivity. An excellent embodiment of such an atomic-sized field sensor is a nitrogen-vacancy (NV) center in diamond [234,313]. The proposals and first proof-of-concept experiments, as well as various experimental and theoretical studies are reviewed in [557].

Figure 4.63a shows a sketch of an NV center, consisting of a substitutional nitrogen atom (N) and a vacancy (V) at one of the nearest neighbor sites of the diamond crystal lattice. The energy level diagram of an NV center is depicted in Fig. 4.63b. The  $^3A_2$  ground level is a spin triplet state, whose sublevels are split by spin-spin interaction into a singlet state of spin projection  $m_s = 0$ , and a doublet with  $m_s = \pm 1$ . The latter is separated by  $D = 2.87$  GHz in the absence of a magnetic field [indicated by the blue arrow in Fig. 4.63b]. A magnetic field  $B_{NV}$  applied along the quantization axis of the NV center  $\mathbf{n}_{NV}$  (the direction of the NV-axis), leads to a splitting of the

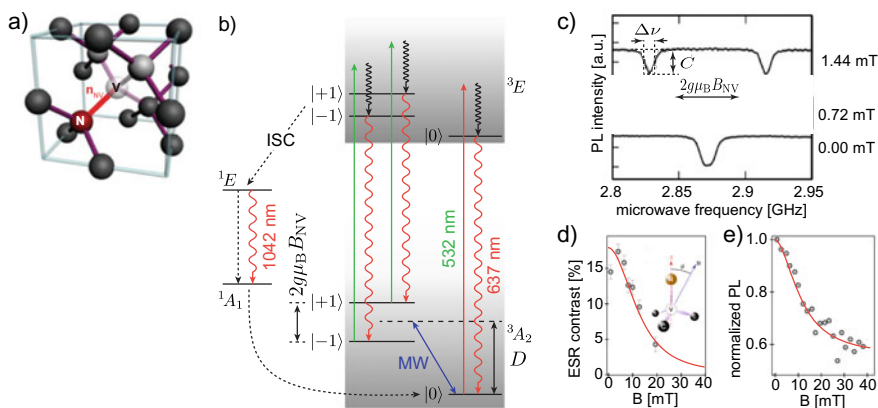


**Fig. 4.63** **a** Atomic structure of the NV defect in diamond. **b** Energy level scheme. The notation  $|i\rangle$  denotes the state with spin projection  $m_s = i$  along the NV defect axis  $\mathbf{n}_{NV}$ . Spin conserving optical transitions from the  $^3A_2$  spin triplet ground state to the  $^3E$  excited state are shown with the green solid arrows. Such transitions are efficiently excited through non-resonant green illumination on the phonon sidebands. The dashed arrows indicate spin selective intersystem crossing (ISC) involving the singlet states  $^1E$  and  $^1A_1$ . The infrared (IR) transition occurring at 1042 nm between the singlet states is also shown. **c** Optically detected electron spin resonance (ESR) spectra recorded for different magnetic field magnitudes applied to a single NV defect in diamond. The ESR transitions are shifted owing to the Zeeman effect, thus providing a quantitative measurement of the magnetic field projection along the NV defect quantization axis. These spectra are recorded by monitoring the NV defect PL intensity while sweeping the frequency of the microwave (MW) field. Spectra for different magnetic fields are shifted vertically for clarity. **d** ESR contrast and **e** normalized PL intensity as a function of magnetic field amplitude applied with an angle  $\theta = 74 \pm 1^\circ$  with respect to the NV defect axis  $\mathbf{n}_{NV}$ . The solid line is the result of a rate equation model developed in [642]. Figure adapted from Rondin et al. [557]. Copyright (2012) IOP Publishing and courtesy of P. Maletinsky

## 4.5.2 SPM Methods Mapping Magnetism at the Atomic Scale

### 4.5.2.1 Spin-polarized Tunneling Microscopy

Since its invention, the scanning tunneling microscope (STM) [81,83] has become an established surface science tool. In an STM, a metallic tip is brought into a close proximity to a conducting sample. At a sufficiently small tip-sample distance, typically below 1 nm, a tunnel current can flow, which depends on the applied bias,  $U$ , on the electronic states of the tip and sample, and exponentially on the tip-sample distance. The tunnel current decays by about one order of magnitude for an increase of the tip-sample distance by 1 Å. This rapid decay ultimately permits to image surfaces with atomic resolution, in spite of the radii of several tens of nanometers typical for STM tips, because most of the tunneling current flows through the apex atom.

An STM can be operated in an imaging mode where the tip-sample distance is adjusted by a feedback such that the measured tunnel current remains constant. Alternatively, the tip can be scanned at constant average height, or with a slow distance feedback, and the variation of the tunneling current arising from the local topography or spatial variations of the local density of states (DOS) can be mapped, provided that the topography is sufficiently small to avoid a tip-sample crash. To explore the electronic states, the dependence of the tunneling current  $I$  on the sample bias  $U$  can be explored. For this, either the dependence  $\frac{dI}{dU}$  on the sample bias  $U$  at a selected tip position  $\mathbf{R}_t$ , or its dependence  $\frac{dI}{dU}$  on the tip position  $\mathbf{R}_t$  at a selected bias  $U$  are recorded to either locally map the electronic states or acquire a spectroscopic image of the sample. Using magnetic tips, the current can become spin-polarized [704] and surface states with different spin-polarization can be distinguished [Fig. 4.66a–c]. Like normal STM, SP-STM can achieve atomic resolution of spin-textures. Examples are shown in Fig. 4.66e and f.

Heinze et. al. [269] used non-polarized and spin-polarized STM tips to image a single Mn monolayer grown pseudomorphically on a W(110) substrate [inset in Fig. 4.66d]. With a non-magnetic STM tip, an atomic resolution image showing the pseudomorphic growth of the Mn on the W(110) substrate is obtained [Fig. 4.66d]. Using an Fe-coated W-tip having an in-plane magnetic moment orientation, the theoretically predicted  $c(2 \times 2)$  AFM superstructure [Fig. 4.66e] was imaged using the constant current mode with a current setpoint of 40 nA and a bias of  $-3$  mV. Generally, SP-STM with atomic resolution of non-periodic structures is however best performed using a spectroscopic imaging mode at a well-selected bias to maximize the spin-polarized term in

$$\left. \frac{dI}{dU} \right|_U \propto n_t n_s(\mathbf{R}_t, \epsilon_F + eU) + \mathbf{m}_t \mathbf{m}_s(\mathbf{R}_t, \epsilon_F + eU), \quad (4.100)$$

where  $\epsilon_F$  is the Fermi energy,  $n_s$ ,  $n_t$ ,  $\mathbf{m}_s$ ,  $\mathbf{m}_t$  are the local density of states of the sample, tip, magnetization density of states of the sample, and tip, respectively [704].

An example of SP-STM with atomic resolution using such as spectroscopic technique was reported by Meier et al. [445] and shown in Fig. 4.66f. The image shows a 3d-representation of data acquired on a sub-monolayer of Co deposited on Pt(111).

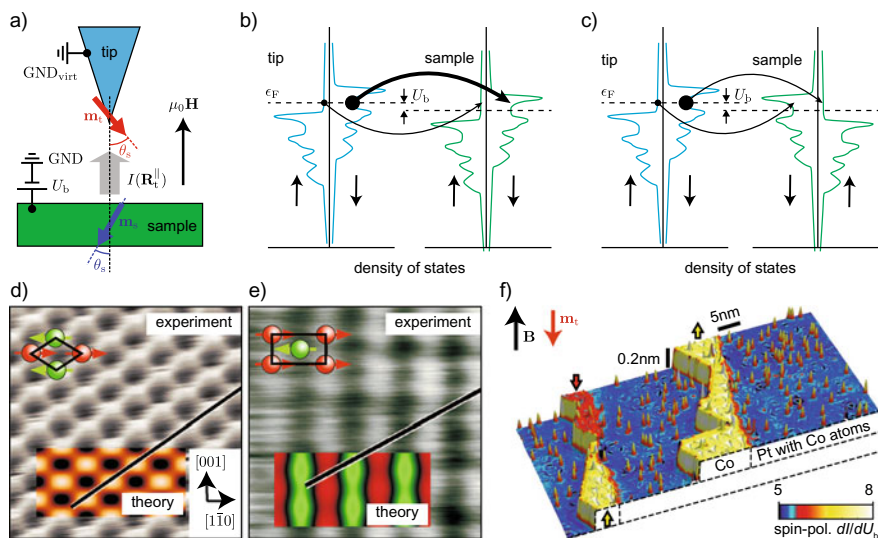


**Fig. 4.66** **a** Schematics of a spin-polarized tip above a magnetic sample in a field  $\mu_0 \mathbf{H}$ . **b** and **c** Electronic states for spin-up and spin-down electrons for a parallel and antiparallel arrangement of  $\mathbf{m}_t$  with  $\mathbf{m}_s$ , respectively. Figure adapted from Phark et al. [519] Copyright 2020, Springer Nature. **d** and **e**  $2 \times 2 \text{ nm}^2$  constant-current STM images of one monolayer of Mn on W(110) imaged with an unpolarized W-tip (**d**) and spin-polarized Fe-coated W-tip (**e**), respectively. While panel **d** reveals the Mn atomic lattice, the data displayed in panel **e** shows the  $c(2 \times 2)$  antiferromagnetic ground state. **f** Shows data obtained on a partial Co layer on a Pt(111) substrate recorded at 0.3 K. The STM topograph is color-coded spectroscopic  $dI/dU$ -data. Figure adapted from Wiesendanger et al. [694]. Copyright 2020, American Physical Society



#### 4.5.2.2 Magnetic Exchange Force Microscopy

With the invention of the atomic force microscope (AFM) [86], or more generally, the scanning force microscope (SFM), a scanning probe microscopy tool to image insulating sample surfaces with highest lateral resolution became available. In their publication, Binnig et al. [86] presented scanlines acquired on an  $\text{Al}_2\text{O}_3$  surface displaying features having a width of about 3 nm. Images showing structures with atomic-scale periodicities were presented a few years later by various groups [22, 87, 449, 450] and it was soon recognized that the images show atomic periodicity. However, atomic-scale defects or unit cell steps with atomic extension perpendicular to the step-edge were never observed. The first images with true atomic resolution were obtained almost a decade after the invention of the AFM by Giessibl [203], Kitamura and Iwatsuki [304], and by the Morita group by Ueyama et al. [657] and Sugawara et al. [628]. For this, the tip is brought into close vicinity to the sample surface such that short-range forces arising from incipient chemical bonds between the tip apex atom and surface atoms occur (see [210] for a review of the earlier work on AFM with atomic resolution). Since 1995, various semiconducting, metallic, and insulating samples have been imaged with atomic resolution. More recently, the controlled functionalization of the tip, either by a CO molecule [231] or by an O atom [464], has become a popular technique to image organic molecules on surfaces.

In case the tip is covered with a magnetic material, the instrument becomes sensitive to the magnetic stray field emanating from the sample surface. However, if the apex atom of an AFM tip coated with a ferromagnetic or antiferromagnetic material is approached sufficiently close to the surface of a magnetic sample, the inter-atomic chemical bonding energy can depend on the relative spin-orientation of the tip apex and surface atom.



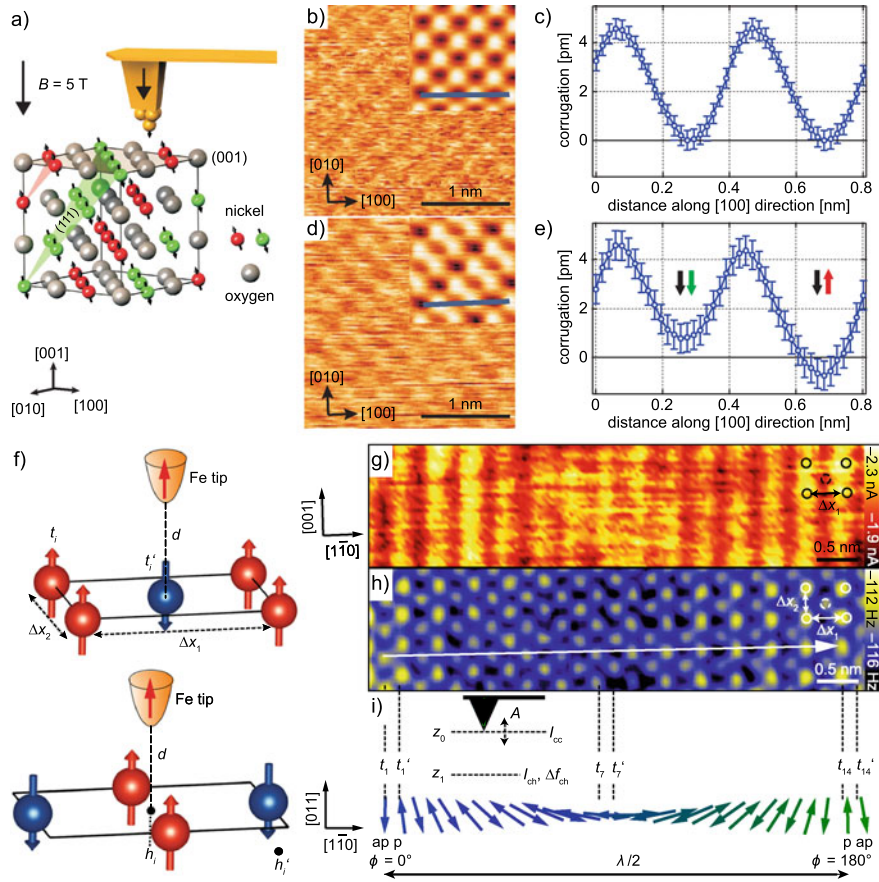


**Fig. 4.68** **a** Concept of MExFM on the insulating antiferromagnetic NiO(001) single crystal. **b** Raw topography data recorded at  $T = 7.6$  K, with a frequency shift kept constant at  $-22$  Hz and unit cell averaged data of the chemical unit cell (inset at the top right). A cantilever with a spring constant of  $\approx 34$  N/m and a free resonance frequency  $f_0 = 159$  kHz was used with an oscillation amplitude  $A = 6.65$  nm at  $U = -1.2$  V. **c** Line section of the spatially averaged magnetic unit cell along the [001]. **d** Raw data measured at  $\Delta f = -23.4$  Hz showing the magnetic unit cell and unit cell averaged data of the chemical unit cell (inset at the top right). **e** Cross-section: an additional apparent height difference between nickel atoms of opposite spin orientations due to the magnetic exchange interaction with the spin of the iron tip is about 1.5 pm. Figure adapted from Kaiser et al. [323]. Copyright 2020, Springer Nature. **f** Sketches of the antiferromagnetic  $c(2 \times 2)$  unit cell which locally approximates the spin spiral. **g** Current  $I_{\text{ch}}$  and **h** frequency shift  $\Delta f_{\text{ch}}$  images of one half of the spin-spiral period [see (i)], measured at constant height ( $z_1$ ) that is by 0.29 nm closer to the surface than the height  $z_0$  at which the current feedback loop was opened ( $U = -10$  mV and  $I_{\text{cc}} = -2$  nA). Parameters: oscillation amplitude  $A = 50$  pm,  $U = -0.1$  mV, tip magnetization normal to the surface. The arrow in **g** depicts the contrast variation due to the reversal of a single spin along the  $[1\bar{1}0]$  direction. **i** Side-view sketch of one half of the cycloidal spin spiral along the  $[1\bar{1}0]$  direction in one monolayer Mn on W(110) together with the experimental measurement scheme. Figure adapted from Hauptmann et al. [261]. Copyright 2020, Springer Nature



## Other Members of the SPM Family

# 5

### Abstract

Members of the family of scanning probe microscopes, be the scanning near-field optical microscopy or electrochemical scanning tunneling microscopy are introduced and some application examples are discussed.

In this chapter, some other members of the scanning probe microscopy family are briefly described. All probe microscopes are based upon probing tips, but some tips are rather different from standard STM tips. Methods such as scanning near-field optical microscopy (SNOM), scanning ion conductance microscopy (SICM) or photoemission microscopy with scanning aperture (PEMSA), are based on tips with apertures, where light, ions or electrons can pass through. The scanning near-field acoustic microscope (SNAM) is the acoustic analogue of the SNOM. Other methods essentially depend on a standard STM feedback and measure outgoing radiation, as in the case of STM with inverse photoemission (STMiP), or measure the influence of incoming light on the tunneling current, as in the case of laser STM (LSTM), or measure the temperature of the tip, as in the case of scanning thermal microscopy (SThM), or perform measurements in an electrolyte, as in the case of electrochemical STM (ECSTM). In scanning noise microscopy (SNM), the noise of the tunneling current is measured at a compensated thermovoltage. In scanning capacitance microscopy (SCM), the capacitance between probing tip and sample is measured. In scanning potentiometry microscopy (SPotM), the electrical potential, which depends on the resistivity of the sample, is measured. In scanning spreading resistance microscopy (SSRM), the spreading resistance is monitored. Scanning tunneling atom probe (STAP) is an example of the combination of STM with a time-of-flight mass spectrometer, where the mass of single ions from the probing tip can be analyzed. TERS is tip enhanced Raman scattering, where plasmons in the nanocavity enhance the electromagnetic fields, where molecular vibrations at the single molecule level can be detected. PIFM means photon induced force microscopy, where light

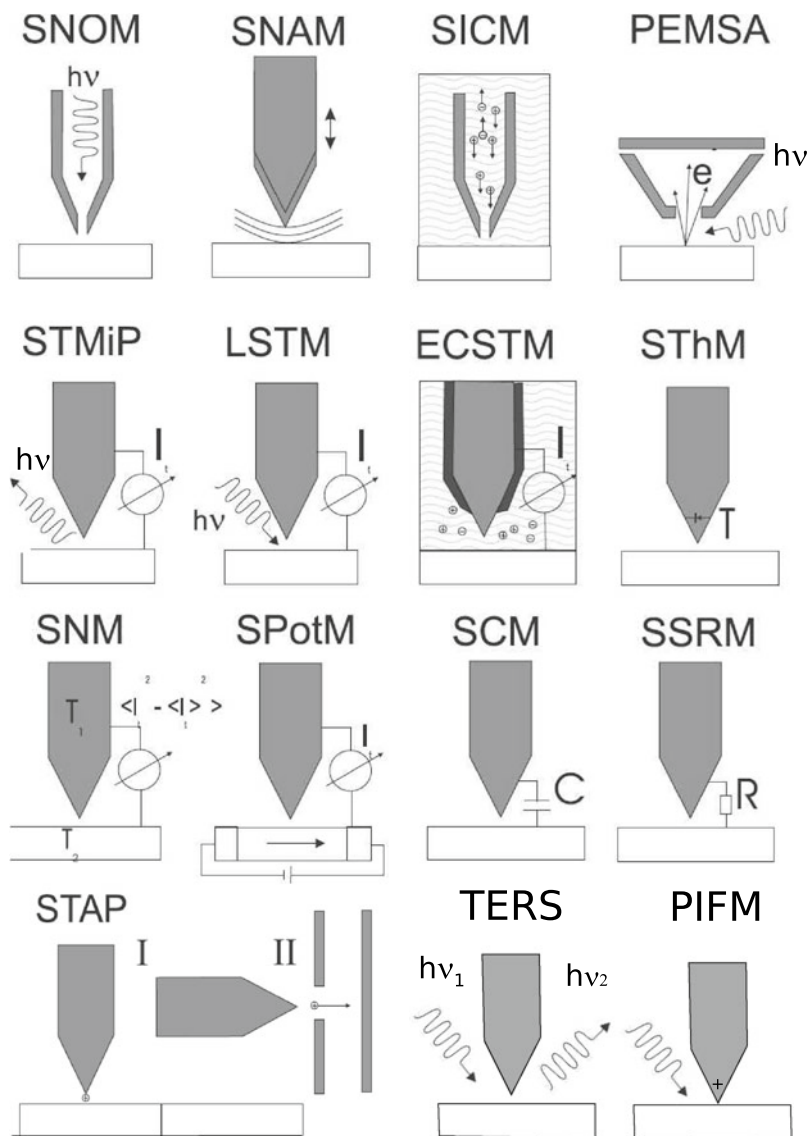


**Fig.5.1** Scanning probe microscopes (see text)

irradiation leads to the creation of image charges, which can be detected by force microscopy. All these modes are schematically depicted in Fig.5.1.



## Abstract

Recurring artifacts in all modes of operation are addressed. Examples are related to the convolution with the tip geometry and the influence of piezo scanner nonlinearities.

## 6.1 Introduction to Artifacts in SPM

In this chapter artifacts of scanning probe microscopy are discussed. The tip artifact, where the sample topography is convoluted with the tip geometry is the most common artifact. A second class of artifacts are topography images, which are influenced by local variations of properties, such as conductance, elasticity, adhesion or friction. The third class of artifacts are local measurements, such as SNOM, STM-induced photoemission or lateral force measurements, which are influenced by local topography. The fourth class of artifacts are instrumental artifacts.

## 6.2 Tip Artifact: Convolution with Tip Shape

The most common artifact in scanning probe microscopy is the tip artifact. It has been observed with STM [213] or SFM [26,238,271,426]. Topographic features, which have a large aspect ratio compared to the probing tip are not correctly reproduced. The acquired image is a convolution between the probing tip shape and the sample feature. A blunt tip will broaden topographic features and reduce corrugation amplitudes. Multiple tips can create “shadows” or repeated features in the images (“ghost images”).

A simple criterion is given by the curvature of the probing tip. All sample features that have a smaller radius of curvature than the radius of curvature of the probing tip are not completely imaged. Commercial manufacturers guarantee a radius of curvature of about 15 nm as an upper bound. In practice, the tip geometry can be

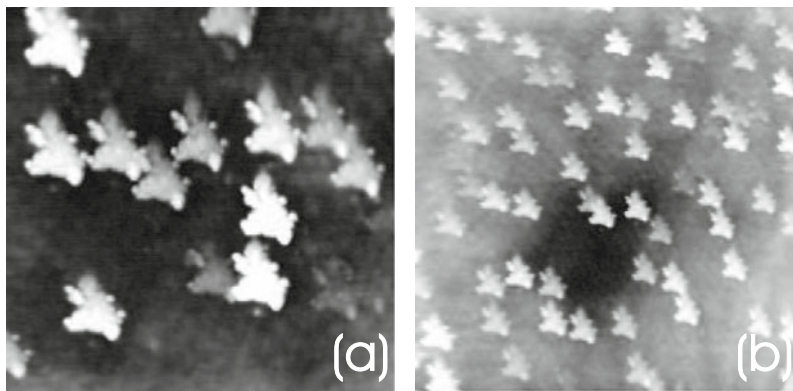


**Fig. 6.1** Observation of tip artifacts with non-contact force microscopy on the  $\text{Al}_2\text{O}_3(0001)$ -surface, where the probing tip is imaged by needle-like structures of the surface. Nanometer-sized mini-tips are observed. The probing tip is a commercially available silicon tip, covered by its native oxide [10]. **a**  $459 \times 459 \text{ nm}^2$ -area, **b**  $918 \times 918 \text{ nm}^2$ -area

rather complicated, including nanometer-sized mini-tips. Therefore, it is advisable to characterize the probing tip with an scanning electron microscope or to image some standard samples, which have needle-like structures. The imaging of these needle-like structures gives a direct image of the probing tip. In Fig. 6.1 sharp needle-like structures are imaged with a non-contact force microscope on the  $\text{Al}_2\text{O}_3(0001)$ -surface.<sup>1</sup> The images show a collection of “islands” that are all identical, which is a clear indication that the probing tip is imaged instead of the needle-like surface feature. Remarkably, the probing tip has several nanometer-sized tips, which yield most probably high resolution on flat parts of the sample.

In the above case, the tip artifact is rather obvious and the tip geometry can be directly determined from the observed image. In this case, the radius of curvature of the tip is much larger than the radius of curvature of the needle-like surface feature ( $R \gg R_s$ ). In addition the spacing between the front-most needles is relatively large. The situation is schematically drawn in Fig. 6.2. Westra et al. could show that SPM images of thin metallic films with columnar structure are often dominated by this tip artifact [689].

In the case, where the tip radius  $R$  is comparable with the spacing between needles or the dimensions of holes ( $R \approx w$  or  $R < w$ ), the situation, as shown in Fig. 6.3, is more complex. Again, the curvature of the SPM profile is given by the radius of curvature of the probing tip  $R$  and can be calculated with the formula of a truncated sphere with the same height  $h$  and width  $w$  as the observed profile:

$$R = \frac{h^2 + (w/2)^2}{2h} \quad (6.1)$$

<sup>1</sup>The sample was heated in ultrahigh vacuum, which led to the formation of needle-like structures.

**Abstract**

Future prospects of scanning probe microscopy are discussed. Arrays of cantilevers can be used for ultrasensitive bio-sensors or be used as a mechanical storage medium. The role of scanning probe microscopy in fields of nanoscience, nanotechnology but also quantum information will be elaborated.

**7.1 Parallel Operation of SFM Cantilever Arrays**

The parallel operation of SFMs has potential in several areas of nanoscale science and technology, such as data storage, lithography, high-speed/large-scale imaging and molecular and atomic manipulation. Minne et al. presented the parallel operation of a 1D array of cantilevers, where the parallel acquisition of images was demonstrated [459]. Ten cantilevers with integrated piezoresistive sensors and zinc-oxide (ZnO) actuators were operated in parallel, where each cantilever scanned a rectangular area of  $200\text{ }\mu\text{m}\times 2\text{ mm}$ . A total area of  $2\text{ mm}\times 2\text{ mm}$  of a memory cell of an integrated circuit was imaged in this way. These scan areas are adapted to the needs of semiconductor industry, where integrated circuit chips of  $100\text{ mm}^2$  are common. Each cantilever provided a resolution in the nm-range with a bandwidth of 20 kHz. The microscope produces such a large amount of data, that it is difficult to be handled by today's processing possibilities. These results clearly show new perspectives for microscopy, where large, complex structures are to be investigated on the nanometer scale. Furthermore, new avenues were opened up in SFM-lithography where patterns on an area of  $1\text{ cm}^2$  were written with line widths in the micron range [459].

A 2-dimensional SFM cantilever array, called “Millipede”, of the IBM Zurich Research laboratory [666] was designed for high density data storage. The “Millipede”-concept is illustrated in Fig. 7.1. A  $32\times 32$  cantilever array is positioned above a polymer surface. The entire cantilever array chip is scanned in x-y-direction. The approach in z-direction is controlled by 3 piezoresistive cantilevers and 3